Title

Performance of a MEMS-based AO-OCT system

ISBN

978-0-8194-7063-8

Authors

Evans, Julia W

Zawadzki, Robert J

Jones, Steve

et al.

Publication Date

2008-02-07

DOI

10.1117/12.771673

Peer reviewed

Performance of a MEMS-based AO-OCT System

Julia W. Evans[a,b], Robert J. Zawadzki[b], Steve Jones[a], Samelia Okpodu[b,c], Scot Olivier[a], John S. Werner[b]

[a]Lawrence Livermore National Laboratory
7000 East Avenue, Livermore 94550
[b]Vision Science and Advanced Retinal Imaging Laboratory, Department of Ophthalmology & Vision Science, University of California, Davis,
Sacramento, CA 95817
[c] Norfolk State University
700 Park Avenue Norfolk, VA 23504

ABSTRACT

Adaptive optics (AO) and optical coherence tomography (OCT) are powerful imaging modalities that, when combined, can provide high-resolution, 3-D images of the retina. The AO-OCT system at UC Davis has been under development for 2 years and has demonstrated the utility of this technology for microscopic, volumetric, *in vivo* retinal imaging. The current system uses a bimorph deformable mirror (DM) made by AOptix Technologies, Inc. for low-order, high-stroke correction and a 140-actuator mirco-electrical-mechanical-system (MEMS) DM made by Boston Micromachines Corporation for high-order correction. We present our on-going characterization of AO system performance. The AO-OCT system typically has residual wavefront error of 100 nm rms. The correctable error in the system is dominated by low-order error that we believe is introduced by aliasing in the control loop. Careful characterization of the AO system will lead to improved performance and inform the design of future systems.

Keywords: Adaptive Optics, MEMS deformable mirror, optical coherence tomography

1. INTRODUCTION

The Adaptive optics (AO)-optical coherence tomography (OCT) system at UC Davis has been under development for 2 years and has demonstrated the utility of this technology for microscopic, volumetric, *in vivo* retinal imaging.[1,2] The combined technology of traditional OCT and adaptive optics provides excellent resolution in all three dimensions. We estimate that our AO-OCT has resolution of $3\mu m^3$.[3] With this level of resolution many of the cellular structures visible in histological images of the retina should be visible, but remain elusive. The limiting factor in AO-OCT images is contrast. High-contrast AO imaging (also know as Extreme AO) is currently an important topic in astronomical imaging. One of the main features of high-contrast AO is an order of magnitude reduction in residual errors of the AO system, in part through rigorous error budget analysis. Improved AO correction in a vision AO system should also increase image contrast, making cellular structures more visible.

Developing an error budget is a common tool for improved performance and system design in astronomical AO systems.[4,5] The process for vision science systems is also discussed in several texts e.g.,[6] but results from this type of analysis have rarely been included in journal articles on AO for vision science. Specifically, compiling an error budget entails an analysis of the sources of residual wavefront error (WFE). The relative size of the sources of residual error will prioritize system upgrades and inform the design of future systems. Ideally an error budget would be calculated for a system in the design phase, but it can also be used to assess and improve performance after construction, as often the difference between designed performance and actual performance is significant. Important tradeoffs for system improvements can also be examined with an error budget. For example increasing the sub-apertures in the AO system can reduce high-order errors and aliasing, but because of reduced light per sub-aperture could increase measurement error. In general, an AO system error budget must include an analysis

Send correspondence to evans74@llnl.gov

MEMS Adaptive Optics II, edited by Scot S. Olivier, Thomas G. Bifano, Joel A. Kubby,
Proc. of SPIE Vol. 6888, 68880G, (2008) · 0277-786X/08/$18 · doi: 10.1117/12.771673

of three categories of residual WFE: errors in measuring the phase, errors caused by limitations of the deformable mirrors (DMs), and errors introduced by temporal variation. In this paper we discuss both the techniques for characterizing these error sources and our measurement of them for the AO-OCT system.

2. SYSTEM DESCRIPTION

An OCT system is basically an interferometer with a sample arm and a reference arm. The AO-OCT system is well described in previous publications (e.g.[2]). The sample arm contains the adaptive optics system and thus is the focus of this paper. It is shown in Fig. 1. The major components of the AO system are the 20 by 20 Shack-Hartman wavefront sensor (S-H WFS), and two deformable mirrors. Spherical mirrors (indicated by S1-S10 in the diagram) re-image the pupil. The system uses an bimorph deformable mirror (DM) made by AOptix Technologies, Inc. for low-order, high-stroke correction[7] and a 140-actuator mirco-electrical-mechanical-system (MEMS) DM made by Boston Micromachines Corporation for high-order correction.[8] These are indicated by DM1 and DM2 in the layout. Like several other imaging modalities, OCT requires the sample arm to scan the retina to produce the science image. Horizontal and vertical scanners are located at pupil planes and indicated by horiz. and vert. in the diagram. For some characterization tasks we can use a model eye, consisting of a lens with a paper 'retina' at the focus. It should be noted that while this sample arm is used for AO-OCT it is very similar to those used for other imaging modalities including AO-scanning laser ophthalmoscopes (SLO). A recent addition to the sample arm is a CCD for measuring the point spread function (PSF) of the system. An additional pellicle beamsplitter was introduced before the splitter for the WFS. Measuring the PSF will allow us to calculate calibration errors in the system and provide another metric of system performance.

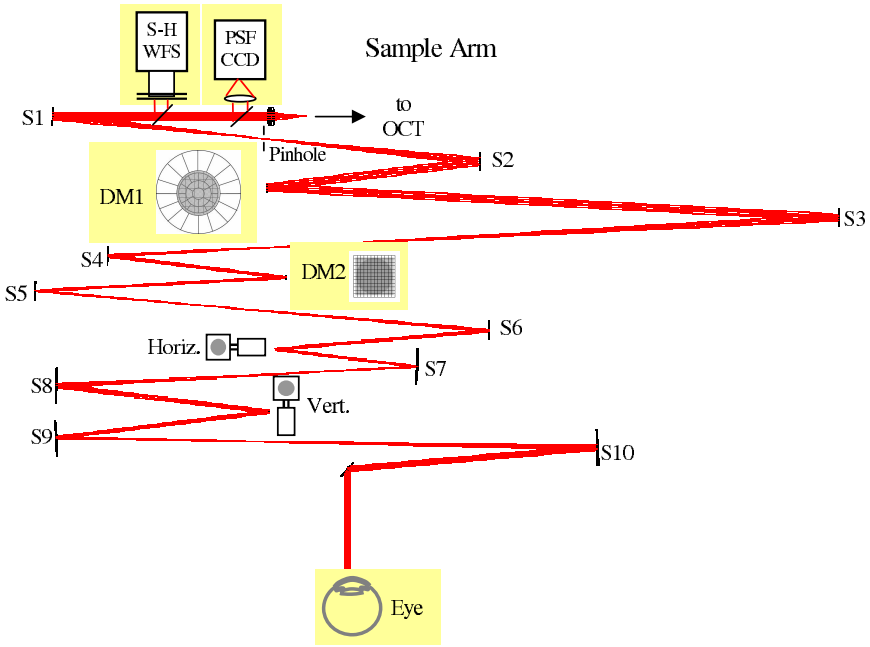

Figure 1. Layout of the AO-OCT sample arm. The system uses a 20 by 20 Shack-Hartmann wavefront sensor, a bimorph deformable mirror for low-order correction and a MEMS deformable mirror for high-order correction. Horizontal and vertical scanners are used to scan the retina. The mirrors indicated by S1 - S10 are spherical mirrors used to re-image the pupil plane. A sample arm like this could also be used for other imaging modalities, like AO-SLO.

An important consideration for a vision system sample arm is light throughput. Light needed for wavefront sensing and imaging is limited by both the amount of light that can safely be delivered to the eye and the limited reflectivity of the eye. There are several light sources for the system. The human subject data presented here were collected with a super luminescent diode (SLD) with a center wavelength of 836 nm and a bandwidth of 112 nm (larger bandwidth sources improve axial resolution). The light budget for the AO-OCT sample arm was calculated using assumed values for reflectivity/transmisivity and then compared to values measured with

a power meter at each focus. Adjustments in the theoretical light budget were made to match experimental measurements generating an accurate system light budget. The system currently delivers approximately 375 μW to the eye with about 29% throughput. The light level is set according to safety standards and not the maximum output of the SLD currently in use. The biggest loss of light occurs at the MEMS DM which has effectively 70% reflectivity. The MEMS mirror is gold coated, however the protective window in front of it has an anti-reflective coating for the visible. Ghost images from the window are significant. The loss of light caused by the addition of the second pellicle for the PSF imaging CCD is a few percent. Presumably the light returning to the WFS experiences the same losses as the input light, but is of course reduced by the reflectivity of the eye. Operating in double pass seems to introduce scattered light from the MEMS device which will be discussed in section 3.4.

As AO performance is the subject of this paper we provide here a brief description of system operation, which should be similar to other AO systems. Prior to closed loop operation the position of the reference centroids and the control matrices for each DM are measured. The reference centroids are measured in 'calibration' mode; A flat mirror is placed in front of S1 and is adjusted to maximize back-coupled light to the input fiber, then the centroid positions are measured. The control matrices (one for each DM) are calculated from the system matrix found by actuating each actuator in the system in single pass mode. In single pass mode a fiber and collimating lens are placed in the eye position and adjusted to maximize the light coupled back to the input fiber used in double pass operation. Typically the bimorph is measured first, then held flat while the MEMS is measured. During closed loop operation the calculated control matrices are used to close the loop on the two DMs consecutively.[2] The double DM configuration is also described for an AO-SLO system in Chen et al.[9] During closed loop operation the rms of centroid displacements is used to gauge performance. During post-processing a Fourier reconstructor is used to examine residual WFE.[10]

3. RESULTS AND DISCUSSION

AO system characterization generally starts with the residual WFE measured by the WFS. Typically this is reported as an rms value, although some groups calculate the PSF from the reconstructed wavefront and use Strehl values as the performance metric. WFE measured by the WFS contains some ambiguities. The reconstructed wavefront is limited by the reconstruction algorithm used— for example a very limited modal reconstruction will underestimate WFE by ignoring high-spatial frequency errors. The WFS measurement itself is limited by the measurement error caused by noise in the CCD, error of the centroiding algorithm, etc. Furthermore the WFS cannot measure all errors that affect performance; calibration and isoplanatic error could be significant and yet unmeasured by the WFS. In spite of these shortfalls the measured residual WFE of the WFS is the fastest way to assess and possibly improve system performance. In the case of the AO-OCT system the WFS is particulary helpful because it is over-sampled compared to correction.

Residual rms WFE for a series of subjects was collected to evaluate system performance. Typical values for good correction are approximately 100 nm rms. The closed loop rms WFE values are shown for three subjects in Fig.2. Two of the subjects have good correction, and one has poor correction (possibly caused by a small aperture). We are interested in both the limitations to good correction and why some subjects have poor correction. The more subjects that can be imaged well, the more robust the scientific results. For the purpose of this discussion we will focus on the limitations to good correction, i.e. the residual error sources that lead to WFE of 100 nm rms.

Not all spatial frequencies measured by the WFS can be corrected by the DMs in the system. The control radius, or the highest-spatial frequency that can be controlled is equal to 1/2 the number of MEMS actuators across the aperture, about 5.5 cycles/aperture. Any WFE (measured or not) with a higher-spatial frequency cannot be corrected and is out-of-band. This type of error is a component of fitting error. Ideally all residual WFE would be out-of-band, because all errors that could be corrected, would be. In practice other error sources limit in-band correction. The model eye, for example has a total WFE of 48 nm rms with 36 nm out-of-band. Subtracting in quadrature indicates that 31 nm rms are still uncorrected in-band. In the human subjects the in-band error is worse. For subject 13 total residual WFE is 78 nm rms, and only 25 nm rms are out-of-band. For the well-corrected subjects included in this study the average WFE is 92 nm rms, with an average of 86 nm rms in-band (31 nm rms out-of-band). One way to understand the distribution of spatial frequencies in residual error is to calculate the power spectrum of the wavefront. Figure 3 compares the radially averaged power spectra of the

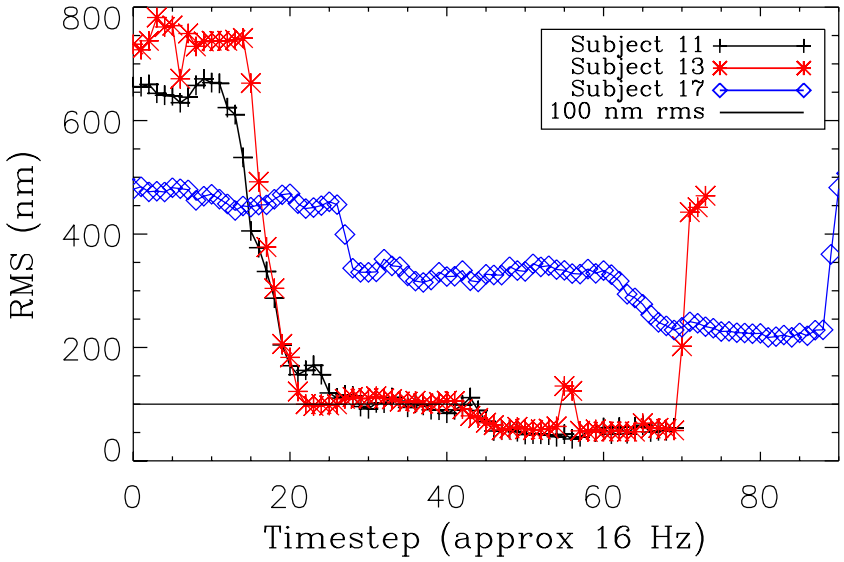

Figure 2. Residual WFE in nm RMS for three subjects. Two of the subjects show typical good correction and the third is representative of a small group of subjects with poor correction. Good correction typically leads to WFEs of about 100 nm rms.

model eye and subject 13. It is immediately obvious that in both cases the residual in-band WFE is mostly low order. These errors should easily be corrected by either the bimorph or the MEMS. In only one of the subjects

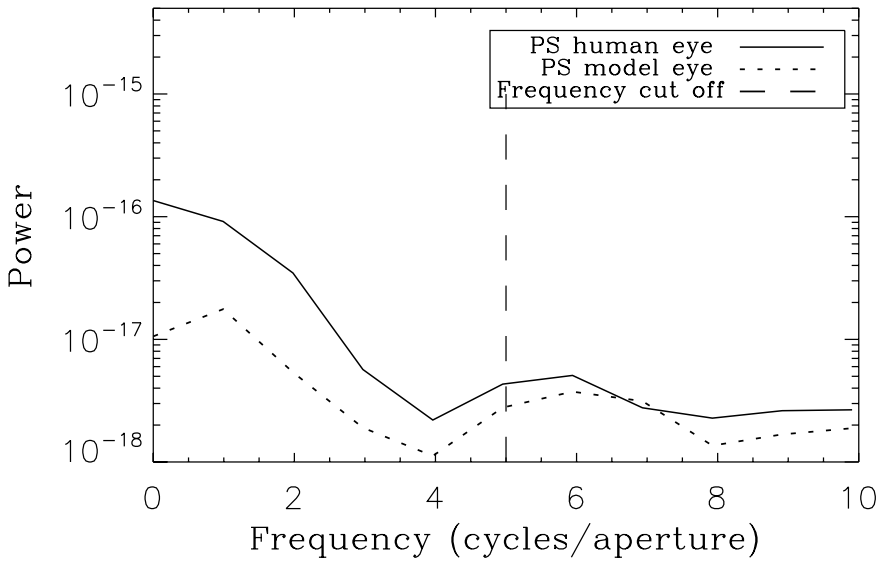

Figure 3. Power spectra for a converged closed loop wavefront of a human subject compared to the model eye. Correctable in-band errors are dominated by low-order error.

(who has excellent vision) were low-order errors not the dominate source of in-band error. Figure 4 compares the power spectra of the uncorrected wavefront for subject 13 to the wavefront after the bimorph correction is

applied and after the MEMS correction is applied (with bimorph still in its corrected position). Low-order errors are reduced by both DMs, but after correction in subject 13 the WFE from 0-2 cycles per aperture is 52 nm rms, and on average this error is 61 nm rms or 70% of in-band error. Identifying and correcting this source of

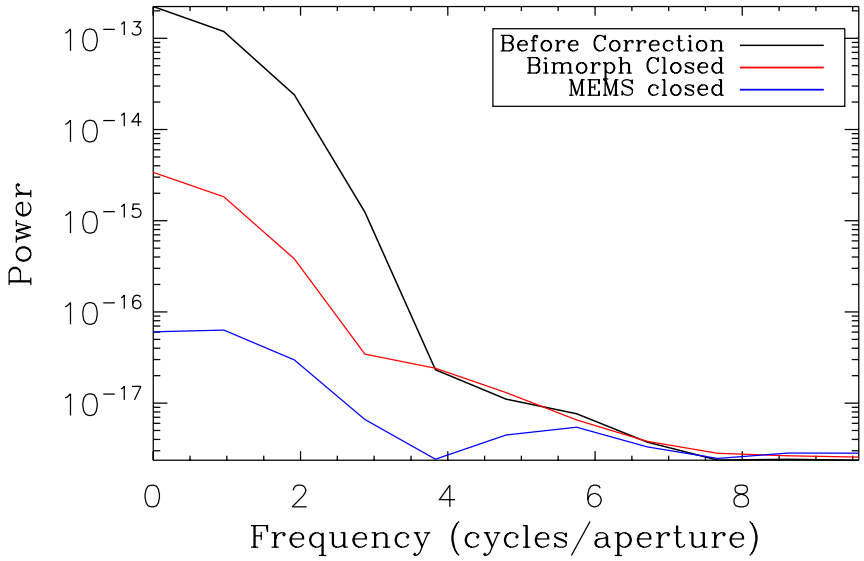

Figure 4. Power spectra of a human subject wavefront, before correction after bimorph correction, and after MEMS correction. The line labeled MEMS closed is the same as in Fig. 3. Low-order residual errors are reduced in each case but remain a large source of error.

low-order error could significantly improve performance as low-order errors can particularly limit image quality. We are working to quantify all sources of residual error in the system. The remainder of this section summarizes our work with a particular emphasis on finding the low-order error discussed here.

3.1 Measurement Error

The ability of the WFS to accurately measure WFE so that it can be corrected is critical to AO performance. In this section we focus on measuring centroid displacements with the WFS. Reconstructing the wavefront from centroid displacements is part of measurement error, but is discussed in the next section. WFS measurement will be limited by noise in the CCD. When the signal is stronger or the CCD noise is lower (i.e. higher signal to noise) the centroiding error is less. Previously we have estimated measurement error from differencing wavefront measurements taken when the system was stable. Using the model eye we estimated measurement error to be 4 ± 2nm rms, which is negligible in the error budget.[11] Centroiding error estimated from the signal to noise of the WFS spots during closed loop operation would be a more accurate way to determine measurement error.

Analytical expressions for calculating centroid error are derived in several papers.[12–14] Currently the AO system uses a thresholded center of mass algorithm for calculating WFS centroids. We calculated centroiding error for each centroid over multiple iterations for a series of subjects. It is difficult to ascribe a single value to centroid error because of the large variation in light levels between subjects and even across the aperture of some individuals. For well-illuminated centroids in subject 13 the average centroid error is ~ 0.05 pixels rms. The average for well-corrected subjects is somewhat higher, 0.1 pixels rms. The average values per centroid for subject 13 are displayed in Fig. 5. Even for this well corrected normal subject there is variation in light levels across the pupil. Note that the image is displayed with a logscale from 0.01 to 0.1. In some subjects there is much higher centroiding error because of poor light levels. The WFS CCD has high read noise (~ 1200 electrons rms/pixel) because it is uncooled producing poor signal to noise in subjects with low-light levels.

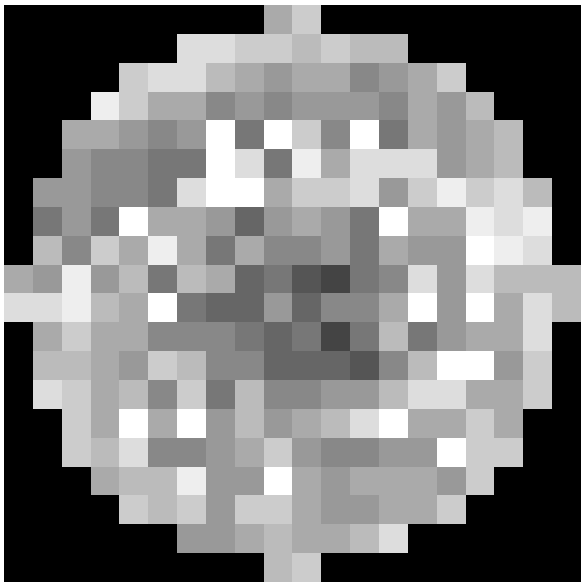

Figure 5. Average calculated centroid error for Subject 13. The image is on a logscale from 0.01 to 0.1 pixels rms. The average error for this subject is 0.05 pixels rms.

Using a gaussian weighted algorithm for centroiding would reduce error an order of magnitude. The algorithm has already been implemented in the AO controller and will be tested in the next months. The new algorithm will probably not improve performance for subjects that are currently well corrected, but hopefully will allow subjects with less reflective eyes (such as older subjects) to be better corrected.

The goal of calculating centroiding error is to confirm the measurement error of the system. The average centroiding error from subject 13 can be input to the Fourier Reconstructor to determine the WFE introduced by centroiding error. The WFE for 0.05 pixels rms centroiding error is about 10 nm rms. This value is not strictly measurement error, because it needs to be reduced by a closed loop averaging factor.[15] The averaging factor will reduce the measurement error by order of a few, producing a measurement error consistent with the measurement error calculating by wavefront differencing. Even in the case of 0.1 pixels rms the reconstructed WFE would be 20 nm rms, a relatively small error compared to the overall error budget.

3.2 Reconstructor Error

During closed loop operations the control matrix previously calculated for each mirror is effectively used to reconstruct the wavefront, also known as Vector Matrix Multiplication (VMM). No complete reconstruction is done, the VMM is used to calculate pseudo-heights, which are converted to voltages to control the mirror. The wavefronts used for the error analysis are generated during post-processing, which differs from the closed loop procedure. During post-processing a Fourier reconstructor is used to estimate the wavefront from the centroid displacements. It is possible that the VMM method is less sensitive to low-order errors or more sensitive to aliasing of higher-order errors than the Fourier Method. In either case the Fourier reconstruction would reveal low-order errors that are not observed (and therefore not corrected) by the control loop. The control matrix for the MEMS is a 12 by 12 matrix, because of the number of actuators on the device, while the Fourier Reconstructor uses all 20 by 20 lenslets on the WFS, making aliasing in the control matrix likely. We can test the reconstructor error by calculating wavefronts with varying spatial frequencies of error, converting these to centroid displacements (slope values) and reconstructing using the two methods. For this analysis we have calculated Fourier and Zernike modes. Figure 6 compares an input signal of a sample Fourier mode and the reconstructed wavefront using the Fourier reconstructor and the MEMS control matrix. The Fourier reconstructor has a small amount of error because of the circular aperture. In this example the input mode is visible in the VMM reconstruction, but in many of the higher-order Fourier modes this is not the case. A similar trend was observed with the Zernike modes. It is not surprising that the MEMS control matrix cannot reproduce all higher-spatial frequency Fourier

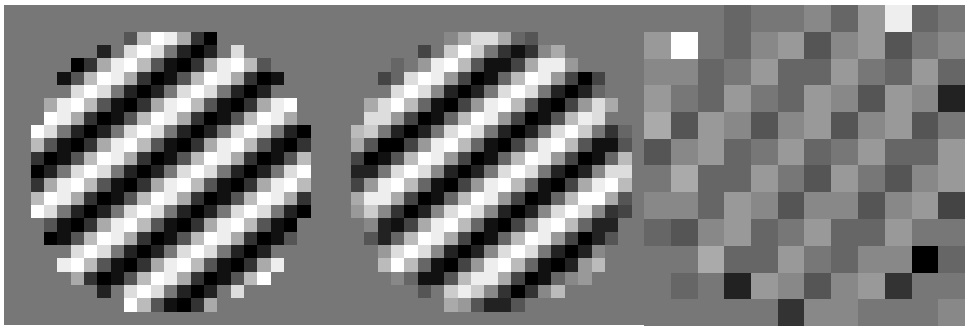

Figure 6. A wavefront with a specific Fourier mode (right) was reconstructed using the Fourier reconstruction (middle) and the VMM reconstruction (left). The VMM reconstruction is not as good as the Fourier reconstruction, but the input mode is still visible. In some of the higher order modes the input mode is completely absent in the VMM reconstruction.

modes, and that in and of itself is not a critical flaw in the system. The control loop does not need to reproduce spatial frequencies that the MEMS cannot correct. The problem arises if the higher-spatial frequency errors are aliased to low-order errors. A comparison of the power spectra from the input signal and the two reconstructed wavefronts reveals that in fact aliasing in the control matrix is a problem. Figure 7 compares the 2-D power spectra of the wavefronts from Fig. 6. The input signal here is not the worst case because the input signal

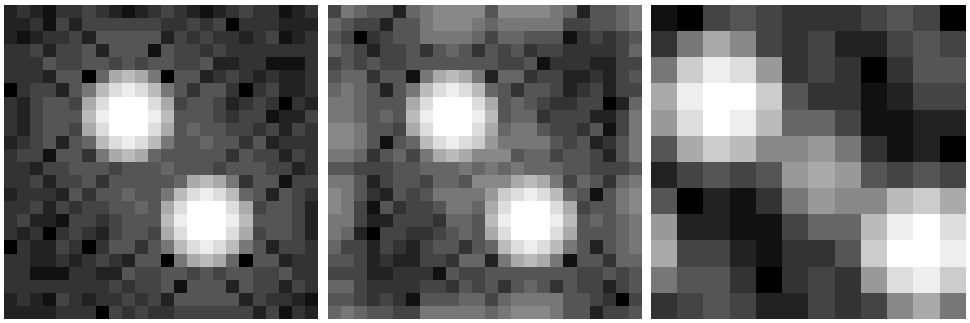

Figure 7. The power spectrum of each of the wavefronts of Fig. 6 is compared above. The slight differences between the power spectra of the input signal and the Fourier reconstruction is because of the circular aperture used (the reconstruction is 'perfect' when a square aperture is used). The VMM power spectra is on a different spatial scale because of the difference in sampling of the wavefront.

is still visible in the VMM reconstruction, however in the power spectra the introduction of low-order error is clear. The difference in scaling of the power spectra is due to the difference in sampling of the wavefronts. It is clear qualitatively from both the Zernike and Fourier mode analysis that the VMM reconstruction does alias high-order errors into low-order errors.

It is difficult to quantify the size of this error because of the difference in sampling and scaling of the reconstructions. In Fig. 8 the VMM reconstruction has been scaled such that the power spectrum has the same max value as the power spectrum from the Fourier Reconstructor. This method is not robust for all of the Fourier Modes tested but can help quantify the effect of aliasing in the control matrix. For this mode the VMM reconstruction introduces 2 orders-of-magnitude more low-order error than the Fourier reconstruction. Low-order error accounts for 70% of in-band (correctable) WFE in the system, making aliasing from the control matrix potentially a significant problem.

It is clear from this analysis that using the VMM of the MEMS DM fundamentally does not allow us to take full advantage of the over-sampled WFS measurement with respect to aliasing. One reason the human subject has more low-order error than the model eye could be that the subject has more high-order error to alias. In the model eye the high-order error will almost exclusively be introduced by print-through of the deformable mirrors, while the human subject will have that error in addition to error from the eye. We will investigate ways to mitigate aliasing in the control loop. One possibility is to use the Fourier Reconstructor during closed loop

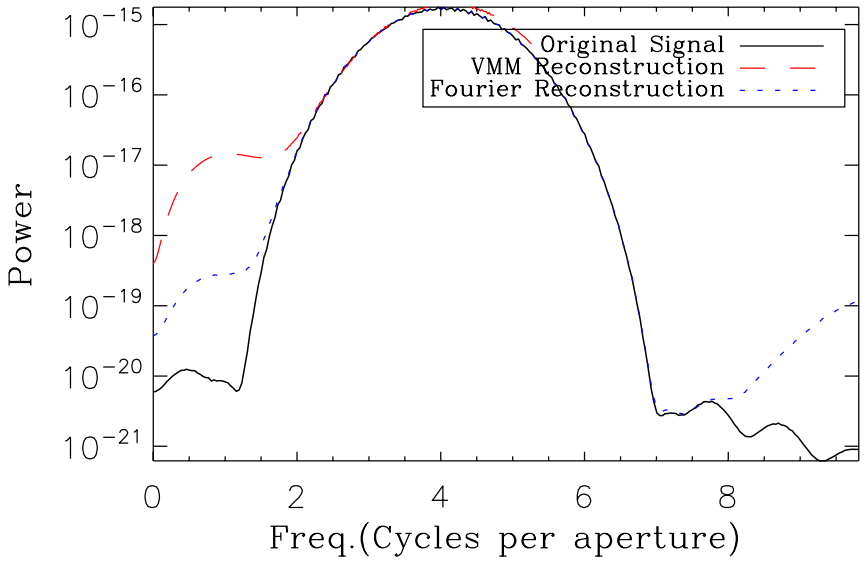

Figure 8. The radial average of the power spectrum of each of the wavefronts of Fig. 6 is compared above. The VMM power spectra has been scaled to have the same peak as the Fourier reconstruction. For this mode (with this scaling) the VMM reconstruction introduces to orders of magnitude more error than the Fourier reconstructor.

operation. The over-sampled WFS measurements will need to be down-sampled to control the MEMS, but using a Fourier reconstruction allows the wavefront to be filtered prior to down-sampling, greatly reducing aliasing.

3.3 Temporal Error

While temporal variation cannot explain low-order residual error in the model eye case, it could be a source of error in human subjects. Temporal variations in the system can be introduced by the limited bandwidth of the AO system. These can be estimated in the same way that measurement error was estimated using the model eye.

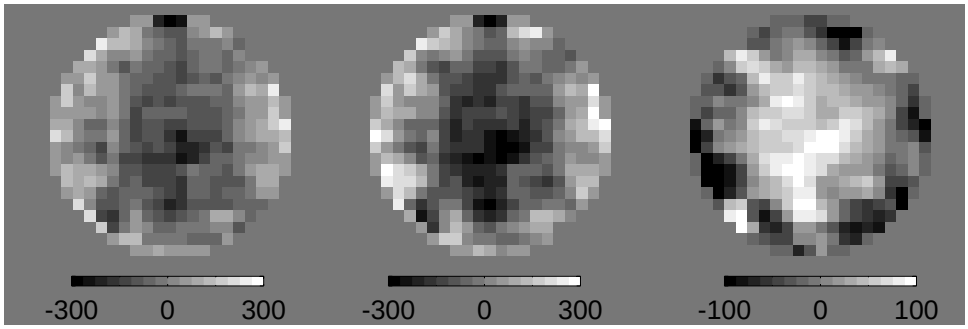

Figure 9. Sample of wavefronts used to calculate bandwidth error for a human subject. Left: Average wavefront from a closed loop archive, Middle: Individual wavefront iteration, Right: Difference between average and iteration. The average rms of the difference between the average wavefront and each iteration is the measurement error plus the bandwidth error, because measurement error is small this value is dominated by the bandwidth error. For well corrected subjects the average bandwidth error is 33 nm rms.

Figure 9 includes a sample of wavefronts used to estimate bandwidth error. On the left is the average converged wavefront from a particular dataset, the middle wavefront is a single iteration and on the right is the difference of the two. The error is the average of the rms differences for all of the converged wavefronts in the dataset. In

this case we are actually calculating the combination of measurement and bandwidth errors, however because measurement errors are small this will be dominated by bandwidth error. We exclude bandwidth error that has out-of-band spatial frequencies as it cannot be corrected. Out of band temporal error should be considered when debating increased sub-apertures in the system. The average bandwidth error for well-corrected human subjects is about 33 nm rms. Aliasing in the control matrix could also be increasing bandwidth errors as small changes in high-order error could change the low-order error which the control loop is incorrectly compensating for. We have recently upgraded the AO control computer and control software, which will allow faster frame rates in the AO system. We will investigate the effect of increased bandwidth on correction.

3.4 MEMS Scatter

The performance of MEMS deformable mirrors has been examined in several contexts.[5,16,17] An important distinction between most MEMS testbeds and the AO-OCT system (as well as other vision systems) is that the AO-OCT sample arm operates in double pass. Both the input and reflected light from the eye are reflected off the MEMS and bimorph DMs. We find that the input light beam back-scatters from the MEMS device into the WFS CCD. This was not observed in many other systems because in single pass mode on-axis back-scattered light would not be measured. In practice the back-scattered light manifests as measured centroids in the WFS when no subject (or model eye) is present in the system. Figure 10 contains three WFS images taken without a subject or model eye in the system. There is a pinhole at the first focus after the input light source that is used to reduce spurious reflections and scattered light in the system. The size of the pinhole affects the appearance and peak value of the back-scattered light from the MEMS. During closed loop operation the pinhole is typically 4 mm, but increasing the pinhole size can improve the dynamic range of the system for correcting defocus. Usually the pinhole size is increased if there is clipping or low light levels then decreased after initial correction with the bimorph. The power levels of these measurements suggest that the back-scattered light could introduce errors

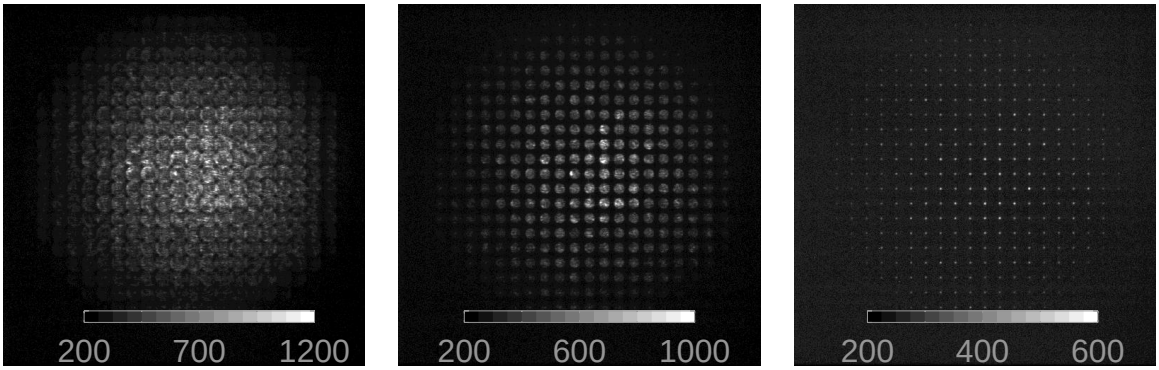

Figure 10. Above are three wavefront sensor images with no subject or model eye in the system. The WFS spots are produced by on-axis back scatter of the input light from the MEMS device. An adjustable pinhole at the first focus position after the light is input is used to block spurious reflections and scattered light in the system for the return path. The size of this pinhole greatly effects the appearance of the back scattered light in the WFS. The image on the left is with the pinhole completely open. The middle image is with the pinhole approximately 4 mm (typical during closed loop operation), and the right image is with the pinhole as small as the iris allows.

in the WFS. Because the pinhole size is frequently adjusted it is difficult to say for any particular subject what the size of the pinhole was. Ideally we would compare WFS images with and without a subject that were taken at the same time. Fortunately during most testing there are frames at the end of the measurement archive when the subject is no longer looking into the system. Figure 11 compares a typical WFS image for Subject 13 during closed loop operation with a measurement from the end of the archive when the subject was no longer looking through the system. In all subjects where data were recorded without the eye this scattered light appears. The WFS measurements without the subject are easy to identify because of the dramatic change in WFE.

Before centroiding is done the WFS images are thresholded. In most of the recent data the threshold was set to 380 counts. This value seemed high based on CCD noise, but was required in practice to get good results.

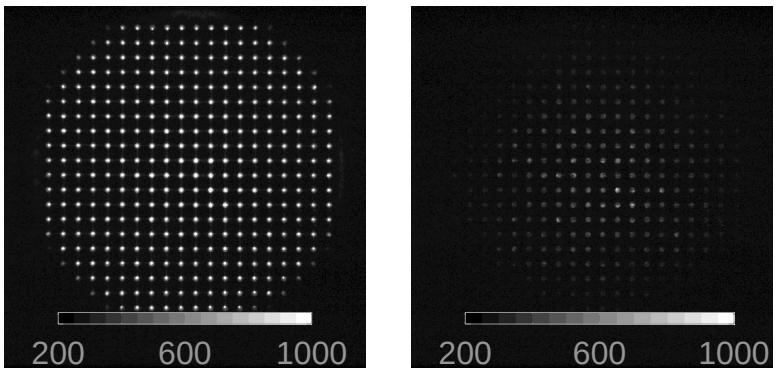

Figure 11. On the left is a typical WFS image during closed loop operation for Subject 13 while on the right is an image from the end of the dataset when the subject was no longer looking into the system (similar to images in Fig.10). The image with the subject looking into the system is saturated because the images are shown on the same scale for comparison.

It seems likely that this threshold level is required to reduce the effect of MEMS scattering on the WFS. In subjects with poor reflectivity the threshold needs to be reduced and in those cases the back-scatter from the MEMS is certainly an issue. Further investigation is needed to understand the contribution of MEMS scatter to residual WFE. It will certainly be dependent on the reflectivity of the subject because while the intensity of the real WFS spots is dependent on the subject the scattered light intensity is dependent only on the input light source, which is relatively constant. Methods to reduce or eliminate this error will also be investigated. If the back-scattered light is relatively stable a software solution might be feasible. Another possibility is to input the light into the eye after the MEMS device so that it is only operated in single pass. This method has been used in other vision systems (though not for the reason described here).[18]

3.5 Calibration Error

One significant flaw of this type of analysis is that the WFE measured by the WFS is relative not absolute. It is dependant on the calibration of the sensor. In general the residual WFE reported for AO systems does not include calibration error, but this error can impact image quality. We plan to estimate WFE from images of the PSF taken with the PSF CCD (See Fig. 1). The camera has been installed and we have obtained first images. It is difficult to compare the measured PSF with the PSF simulated from the measured wavefront because of poor sampling of the wavefront. This is further complicated in calibration mode because there is very little WFE to aberrate the PSF. We are investigating phase retrieval methods to calculate the wavefront from the measured PSF (or a slightly out of focus PSF) for comparison to the WFS reconstructed wavefront.

4. CONCLUSIONS AND FUTURE WORK

AO system characterization is often an iterative process. As error sources are identified, attempts are made to reduce them. The goal is generally improved system performance and ultimately better science images. It is important to understand the relative size of errors to direct limited time and funds towards correcting the most egregious errors. In this AO-OCT system aliasing in the control loop appears to be the most significant error source for well-corrected subjects. We have presented our continuing analysis of the residual WFE as measured by the WFS, the next important step is to analyze errors not measured by the WFS, especially calibration errors.

ACKNOWLEDGMENTS

The authors would like to thank Lisa Poyneer for her helpful advice regarding errors in reconstruction. This work performed under the auspices of the U.S. Department of Energy by Lawrence Livermore National Laboratory under Contract DE-AC52-07NA27344. This research was supported by the National Eye Institute (grant EY 014743). This work was supported by funding from the National Science Foundation. The Center for Biophotonics, an NSF Science and Technology Center, is managed by the University of California, Davis, under Cooperative Agreement No. PHY 0120999.

REFERENCES

1. R.J. Zawadzki, S. Jones, S. Olivier, M. Zhao, B. Bower, J. Izatt, S. Choi, S. Laut, and J. Werner, "Adaptive-optics optical coherence tomography for high-resolution and high-speed 3D retinal in vivo imaging," *Optics Express* **13**(21), pp. 8532–8546, 2005.
2. R.J. Zawadzki, S. Choi, S. Jones, S. Oliver, and J.S. Werner, "Adaptive optics-optical coherence tomography: optimizing visualization of microscopic retinal structures in three dimensions," *Journal of the Optical Society of America A* **24**(5), pp. 1373–1383, 2007.
3. R.J. Zawadzki, Y. Zhang, S. Jones, R. Ferguson, S. Choi, B. Cense, J.W. Evans, D. Chen, D. Miller, S. Olivier, *et al.*, "Ultrahigh-resolution adaptive optics-optical coherence tomography: toward isotropic 3 μm resolution for in vivo retinal imaging."
4. M. van Dam, D. Le Mignant, and B. Macintosh, "Performance of the Keck Observatory Adaptive-Optics System," *Applied Optics* **43**(29), pp. 5458–5467, 2004.
5. J. W. Evans, B. A. Macintosh, L. Poyneer, K. Morzinski, S. Severson, D. Dillon, D. Gavel, and L. Reza, "Demonstrating sub-nm closed loop MEMS flattening," *Optics Express* **14**, pp. 5558–5570, 2006.
6. J. Porter, H. Queener, J. Lin, K. Thorn, and A. A. S. Awwal, *Adaptive Optics for Vision Science Principles, Practices, Design, and Applications*, Wiley-Interscience, 2006.
7. D. A. Horsley, H. Park, S. Laut, and J.S. Werner, "Characterization of a bimorph deformable mirror using stroboscopic phase-shifting interferometry," *Sensors and Actuators A: Physical* **134**, pp. 221–230, 2007.
8. T. Bifano, P. Bierden, and J. Perreault, "Micromachined deformable mirrors for dynamic wavefront control," in *Advanced Wavefront Control: Methods, Devices and Applications II*, J. D. Gonglewski, M. T. Gruineisen, and M. K. Giles, eds., *Proc. SPIE* **5553**, pp. 1–16, 2004.
9. D. Chen, S. Jones, D. Silva, and S. Olivier, "High-resolution adaptive optics scanning laser ophthalmoscope with dual deformable mirrors," *Journal of the Optical Society of America A* **24**(5), pp. 1305–1312, 2007.
10. L. Poyneer, D. Gavel, and J. Brase, "Fast wave-front reconstruction in large adaptive optics systems with use of the Fourier transform," *Journal of the Optical Society of America A* **19**(10), pp. 2100–2111, 2002.
11. J.W. Evans, R. J. Zawadzki, S. Jones, S. Olivier, and J. S. Werner, "Characterization of an AO-OCT system," in *Adaptive Optics For Industry and Medicine Proceedings of the Sixth International Workshop* edited by Christopher Dainty (National University of Ireland, Galway, Ireland & Imperial College, London, UK) Imperial College Press, 2008.
12. M. Nicolle, T. Fusco, G. Rousset, and V. Michau, "Improvement of Shack-Hartmann wave-front sensor measurement for extreme adaptive optics," *Optics Letters* **29**(23), pp. 2743–2745, 2004.
13. P. Prieto, F. Vargas-Martín, S. Goelz, and P. Artal, "Analysis of the performance of the Hartmann-Shack sensor in the human eye," *Journal of the Optical Society of America A* **17**(8), pp. 1388–1398, 2000.
14. K. Baker and M. Moallem, "Iteratively weighted centroiding for Shack-Hartmann wave-front sensors," *Optics Express* **15**(8), pp. 5147–5159, 2007.
15. S. Olivier, C. Max, D. Gavel, and J. Brase, "Tip-tilt compensation- Resolution limits for ground-based telescopes using laser guide star adaptive optics," *Astrophysical Journal* **407**(1), pp. 428–439, 1993.
16. N. Doble, G. Yoon, L. Chen, P. Bierden, S. Oliver, and D. R. Williams, "Use of a microelectricalmechanical mirror for adaptive optics in the human eye," *Optics Letters* **27 No. 17**, pp. 1537–1539, 2002.
17. J.W. Evans, S. Thomas, D. Dillon, D. Gavel, D. Phillion, and B. Macintosh, "Amplitude variations on the ExAO testbed," in *Techniques and Instrumentation for Detection of Exoplanets III*, D. R. Coulter, ed., *Proc. SPIE* **6693**, p. 669312, 2007.
18. D. Hammer, R. Ferguson, C. Bigelow, N. Iftimia, T. Ustun, and S. Burns, "Adaptive optics scanning laser ophthalmoscope for stabilized retinal imaging," *Optics Express* **14**(8), pp. 3354–3367, 2006.